JCTC Journal of Chemical Theory and Computation

ARTICLE

pubs.acs.org/JCTC

Distinct Morphologies for Amyloid Beta Protein Monomer: $A\beta_{1-40}$, $A\beta_{1-42}$, and $A\beta_{1-40}$(D23N)

Sébastien Côté,[†] Philippe Derreumaux,[‡] and Normand Mousseau*,[†]

[†]Département de Physique and Groupe de Recherche Sur Les Protéines Membranaires (GEPROM), Université de Montréal, C.P. 6128, succursale Centre-ville, Montréal (Québec), Canada

[‡]Laboratoire de Biochimie Théorique, UPR 9080 CNRS, Institut de Biologie Physico Chimique, Institut Universitaire de France, Université Paris Diderot - Paris 7, 13 rue Pierre et Marie Curie, 75005 Paris, France

ABSTRACT: Numerous experimental studies indicate that amyloid beta protein ($A\beta$) oligomers as small as dimers trigger Alzheimer's disease. Precise solution conformation of $A\beta$ monomer is missing since it is highly dynamic and aggregation prone. Such a knowledge is however crucial to design drugs inhibiting oligomers and fibril formation. Here, we determine the equilibrium structures of the $A\beta_{1-40}$, $A\beta_{1-42}$, and $A\beta_{1-40}$(D23N) monomers using an accurate coarse-grained force field coupled to Hamiltonian-temperature replica exchange molecular dynamics simulations. We observe that even if these three alloforms are mostly disordered at the monomeric level, in agreement with experiments and previous simulations on $A\beta_{1-40}$ and $A\beta_{1-42}$, striking morphological differences exist. For instance, $A\beta_{1-42}$ and $A\beta_{1-40}$(D23N) have higher β-strand propensities at the C-terminal, residues 30−42, than $A\beta_{1-40}$. The D23N mutation enhances the conformational freedom of the residues 22−29 and the propensity for turns and β-strands in the other regions. It also changes the network of contacts; the N-terminal (residues 1−16) becoming more independent from the rest of the protein, leading to a less compact morphology than the wild-type sequence. These structural properties could explain in part why the kinetics and the final amyloid products vary so extensively between the $A\beta_{1-40}$ and the $A\beta_{1-40}$(D23N) peptides.

1. INTRODUCTION

Alzheimer's disease (AD) is characterized by the presence of extracellular neuritic plaques and intracellular neurofibrillary tangles in the brain.[1] Senile plaques are made of the amyloid beta ($A\beta$) protein. This protein is naturally produced through the cleavage of the amyloid precursor glycoprotein (APP) by the β- and γ-secretases. Many alloforms with amino acid lengths varying between 39 and 43 are produced. Of these, $A\beta_{40}$ is the most abundant, and $A\beta_{42}$ is the most toxic and aggregation prone.[2]

Experimental studies using circular dichroism (CD) spectroscopy and electron microscopy[3] indicate that $A\beta$ peptides exhibit a transition from random coil to β-sheet during fibrillation. Other experiments reveal that the final amyloid product, the nucleation and elongation rates[4] are distinct for different alloforms and are modulated by experimental conditions.[5] The oligomerization pathways also vary for different alloforms[6,7] and $A\beta$ oligomers, rather than the amyloid fibrils, are the principal neurotoxic agents[2,8] interacting with receptors,[9] metal ions,[10] cell membranes,[11] and synapses.[12] Despite these significant advances in $A\beta$ amyloid fibril assembly, precise aqueous solution conformations of $A\beta$ monomer are missing. We know from solution NMR that it is mostly coil turn with little β-strand content in water solution,[13,14] that $A\beta_{42}$ is more structured at the C-terminal than $A\beta_{40}$,[15] and that oxidation of Met35 causes important changes in the monomer structure.[16] Also, hydrogen/deuterium exchange experiments showed that the monomer is completely exposed to the solvent, revealing that it is highly fluctuating.[17] Finally, limited proteolysis/mass spectrometry on $A\beta_{40}$ monomer suggests many turns, such as between Val24 and Lys28, which was observed by solution NMR on the $A\beta_{21-30}$ fragment.[18]

Yet detailed conformational knowledge of $A\beta$ monomer is of utmost importance for two reasons. First, the monomer exists in equilibrium with oligomers during polymerization,[6] interacts with the cell membrane,[11] binds to fibril,[19] and may even be neuroprotective.[20] Second, since $A\beta$ oligomers as small as dimers have been implicated in AD,[21] it is important to block oligomerization at the monomer level. To complement biophysical studies, computer simulations are often used. Several molecular dynamics (MD) simulations have already been reported on $A\beta_{40}$[22] and $A\beta_{42}$[23] folding in aqueous solution. Other studies examined the role of ion binding,[24] oxidation of Met35,[25] and salt bridge Asp23-Lys28[26] on the folding of $A\beta$ monomers. These simulations revealed many interesting features, but the generated conformational ensemble is affected by the starting structure used and by the short time scale explored. Moreover, MD simulations easily get trapped in local minima biasing the results when the energy landscape is rugged, as is the case with $A\beta$.

Replica exchange molecular dynamics (REMD) simulation, which enhances conformational sampling,[27] has also been used. For the monomer of $A\beta_{40}$ and $A\beta_{42}$, it was coupled to different all-atom force fields with explicit[28] and implicit solvent models.[29] Each replica was however simulated for 60−100 ns,[28,29] which may not be enough to sample the complete morphological ensemble. This convergence problem certainly holds for the simulation of $A\beta_{1-39}$.[30] A recent extensive all-atom simulation with implicit solvent on the truncated $A\beta_{10-40}$ monomer reached convergence.[31] However, the predicted percentage of α-helix

Received: September 21, 2010
Published: June 14, 2011

dx.doi.org/10.1021/ct1006967 | J. Chem. Theory Comput. 2011, 7, 2584–2592

content (~38%) is significantly overestimated compared to the CD analysis (between 9 and 12%[3,32]) and the weak α-helix signal detected by NMR.[13] In addition, the N-terminal segment must not be discarded as it has been recently recognized that mutations at positions 6 and 7 alter monomer folding and oligomerization.[33] Finally, two long all-atom simulations based on different force fields and sampling approaches were recently performed on the $A\beta_{42}$ monomer. They reported, however, very different conformational ensembles: with high β-sheet content and forming, for instance, a four-stranded antiparallel β-sheet using Monte Carlo simulated annealing and an implicit solvent[34] or an ensemble of predominantly random coil conformations from a 225 ns REMD simulation using AMBER force field with explicit solvent.[35]

These divergent computational conclusions on the nature of the conformations that characterize the whole ensemble of $A\beta_{40}$ and $A\beta_{42}$ monomer motivated us to re-explore their foldings using a different approach. Here, we use the coarse-grained protein force field (OPEP), which has been tested on widely different systems,[36] and we couple it to a hybrid of Hamiltonian and temperature replica exchange molecular dynamics (HT-REMD),[37] which allows a more efficient sampling of the conformational space than standard temperature REMD. Along the wild-type $A\beta_{40}$ and $A\beta_{42}$ peptides, we also examined the $A\beta_{40}$-(D23N) variant implicated in early onset AD.[38] To our knowledge, there is no experimental and computational study on the $A\beta_{40}$(D23N) monomer. Yet, the mutation D23N has strong consequences on polymerization and fibril product. While the kinetics of $A\beta_{40}$ and $A\beta_{42}$ polymerization shows a lag phase, with $A\beta_{42}$ peptide forming fibrils at a much faster rate, the $A\beta_{40}$-(D23N) peptide does not display any lag phase.[39] In addition, $A\beta_{40}$ and $A\beta_{42}$ form in-register parallel β-sheet fibrils,[40−42] whereas $A\beta_{40}$(D23N) predominant fibrils form antiparallel β-sheets.[39] Such fibrillar morphologies are usually seen only for short sequences making therefore $A\beta_{40}$(D23N) a very special alloform.

2. METHODOLOGY

We use the implicit coarse-grained potential OPEP 3.2 parameter set[36] coupled with HT-REMD[37] to describe the morphologies visited by $A\beta_{1-40}$, $A\beta_{1-42}$, and $A\beta_{1-40}$(D23N) alloforms using the same protocol. $A\beta_{40}$ has the following amino acid sequence: DAEFRHDSGYEVHHQKLVFFAEDVGSNKGAIIGLMVGGVV. For $A\beta_{42}$, two more residues, Ile41 and Ala42, are present at the C-terminal end, and for $A\beta_{40}$(D23N), the positively charged residue Asp23 is mutated into the neutral Asn23. We use 23 temperatures following an exponential distribution: 200.0, 229.7, 239.9, 259.4, 261.5, 273.1, 285.1, 297.7, 310.8, 324.6, 338.9, 353.9, 369.5, 385.8, 402.8, 420.6, 439.2, 458.6, 478.6, 500.0, 502.0, 504.0, and 505.0 K. At the highest temperature, we use a potential reduction scale composed of 5 steps: 0.8, 0.7, 0.6, 0.4, and 0.2 that fractionally reduces nonbonded attractive forces. Exchanges between neighboring replicas are attempted every 7.5 ps resulting in an exchange rate of 50−60%. This relatively high exchange rate is due to the use of a coarse-grained protein model coupled with an implicit solvent, which decreases the effective number of degrees of freedom, and to the low secondary structure probability of the peptides, as discussed in Section 3. In the absence of clear structural differences, configurational energies between nearby temperatures tend to be closer.

Bond lengths are constrained with the RATTLE algorithm.[43] The simulations are thermalized using Berendsen's thermostat with a coupling constant of 0.1 ps[44] and have an integration time step of 1.5 fs. Simulations are started from a random extended conformation with an end-to-end distance of 36.9, 37.5, and 36.9 Å for $A\beta_{1-40}$, $A\beta_{1-42}$, and $A\beta_{1-40}$(D23N), respectively. Each monomer is simulated in a sphere of 60 Å radius with reflecting boundary conditions. The size chosen for the sphere minimizes boundary conditions bias. Each replica of $A\beta_{1-40}$ is simulated for 700 ns (giving 19.6 μs total time), each replica of $A\beta_{1-42}$ for 900 ns (giving 25.2 μs total time), and each replica of $A\beta_{1-40}$(D23N) for 900 ns (giving 25.2 μs total time). These extensive simulations are necessary to reach convergence as discussed below.

Potential. We choose the implicit solvent coarse-grained potential optimized potential for efficient structure prediction (OPEP) 3.2 because it captures the main interactions during protein folding without costing much computational time, such as an all-atom explicit solvent potential.[36] This potential has been shown to recover the native structure of a variety of peptides with widely different secondary and tertiary structures as accurately as all-atom potentials using temperature REMD simulations.[45] OPEP has also been applied to short and long amyloid sequences giving results with strong similarities with experiments.[37,46−51] Coupled to a greedy algorithm and a structural alphabet, OPEP was able to locate, using a benchmark of 25 peptides with 9−23 amino acids, lowest energy conformations differing by 2.6 Å Cα root-mean-square deviation (rmsd) from the full NMR structures.[52,53] Briefly, this model approximates each amino acid by 6 beads: N, H_N, C_α, SC, C, and O, where the side chain (SC) is represented by a unique bead with glycines having a H instead of SC. The interaction parameters are finely tuned against protein structures and thermodynamics and include bond lengths and angles, improper torsions, dihedral angles, van der Waals interactions, and two- and four-body cooperative hydrogen bonds.

HT-REMD. In order to determine the conformations of $A\beta$, we use an hybrid of Hamiltonian and temperature replica exchange molecular dynamics (HT-REMD). T-REMD is widely used to simulate protein aggregation with a variety of implicit and explicit solvents.[27] Nonetheless, for some proteins, it is observed that T-REMD alone is not sufficient to completely unfold the protein and escape from strong local minima. HT-REMD enhances sampling by reducing nonbonded attractive forces at the highest temperature.[37] This allows $A\beta$ to unfold completely into an extended chain.

As T-REMD,[27,45] HT-REMD has a distribution of temperatures allowing exchanges between neighboring replicas i and j according to the Metropolis criterion that preserves thermodynamic ensembles:

$$Prob(i \leftrightarrow j) = min\left\{1, exp\left[\frac{E_i - E_j}{k_B(T_i - T_j)}\right]\right\} \quad (1)$$

where $Prob(i \leftrightarrow j)$ is the probability of exchange between replicas i and j, E_i and E_j are the energies of replicas i and j, respectively, and T is the temperature.

As H-REMD,[54] HT-REMD possesses an energy scale at the highest temperature in which nonbonded attractive forces are fractionally reduced. Exchanges between neighboring replicas i and j are governed by

$$Prob(i \leftrightarrow j) = min\left\{1, exp\left[-\frac{H_i(X') - H_i(X) + H_j(X) - H_j(X')}{k_B T_{max}}\right]\right\} \quad (2)$$

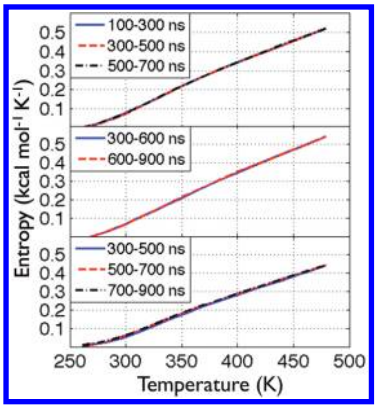

Figure 1. Entropy as a function of temperature $S(T)$ averaged over different time intervals. Aβ_{40}, Aβ_{42}, and Aβ_{40}(D23N) are shown in the top, middle, and bottom panels, respectively.

where H denotes the Hamiltonian (energy) and X and X' are the configurations of replicas i and j, respectively. By decreasing the nonbonded attractions between atoms at the highest temperature, HT-REMD helps the replicas escape from deep local minima increasing the conformational space sampling.

Analysis. We analyze the secondary and tertiary structures at 325 K as justified in Section 3.2 using the equilibrated time interval of each alloform. The secondary structure is analyzed using STRIDE,[55] and the tertiary structure is analyzed using contacts between side chains and clustering. Contacts are considered when the distance between two side chain beads is smaller than the sum of their van der Waals radii plus 0.5 Å. For clustering, we first calculate the rmsd between all structures for each alloform. We then find the biggest cluster, remove from the pool of structures all those contained in this cluster, and repeat iteratively until no structure is left.[56] We select a small threshold of 2 Å C_α rmsd to increase the discrimination between clusters.

The weighted histogram analysis method[57] is used to calculate the free energy, and the entropy is calculated using $S = (E - F)/T$. J-coupling constants between H_N and H_α, $^3J_{H_\alpha H_N}$, are calculated using the Karplus equation[58] with three different sets of coefficients.[35,59,60] Error bars for the J-coupling constants and the secondary structure propensities show the interval of confidence on the mean value given by the bootstrap statistical analysis method.[61]

Convergence. Convergence in our simulations is assessed by three criteria. First, we check that, at equilibrium and based on the ergodic principle, the entropy as a function of temperature, $S(T)$, is time independent when averaged over sufficiently long periods as is seen in Figure 1. Aβ_{40} is the most rapidly converged simulation, and $S(T)$ converges within 200 ns time intervals after only 100 ns of equilibration. As Aβ_{42} converges more slowly, the equilibration takes 300 ns, and the entropy becomes time independent when averaged over 300 ns time windows. Aβ_{40}(D23N) requires an equilibration time of 500 ns, and $S(T)$ remains constant within 200 ns time windows. Note that the differences in the time windows to reach equilibrium and obtain converged entropies starting from similar conformations for the three alloforms cannot be related to differences in aggregation properties. They only indicate that the configuration space of Aβ_{42} is more complex than those of Aβ_{40} and Aβ_{40}(D23N). We further note that the entropy of the three alloforms has a similar slope, which is related to their weak secondary structure signals and their overall behavior as random coil polymers. Second, to further confirm convergence, we look at the variation of secondary structure using the time windows mentioned above for each alloform. The same trend is observed in each time window, and the probabilities of secondary structures per residue vary on average by only 4−5% implying convergence (data not shown). Third, as a final check, we cluster all structures in each time window for each alloform and find that the resulting distribution of clusters is very similar between different time windows. These results confirm that, with our simulation protocol, each alloform has fully converged. As a result, for analysis, we use the equilibrated time interval of each alloform: from 100 to 700 ns for Aβ_{40}, 300 to 900 ns for Aβ_{42}, and 500 to 900 ns for Aβ_{40}(D23N), totaling 80 000, 80 000, and 53 333 structures, respectively.

Naming Convention. To facilitate analysis, the sequence is often split into four regions: the N-terminal (residues 1−16), the central hydrophobic core or CHC (residues 17−21), the loop region (residues 22−29), and the C-terminal (residues 30−42). The N-terminal is mostly hydrophilic, the CHC corresponds to[17] Leu-Val-Phe-Phe-Ala (LVFFA),[21] the loop region refers to the residues forming a loop in the fibrillar morphologies, and the C-terminus is mostly hydrophobic.

3. RESULTS

3.1. J-Couplings. Before comparing the properties of the three alloforms, it is important to select the appropriate simulation temperature for comparison with experiments. It is known that even all-atom simulations with explicit solvent generally show a shift between the predicted and experimentally observed melting temperatures, indicating that the comparison between computation and experiments cannot be made directly with the temperature used in the experiments.[62] This feature has also been observed with the OPEP force field.[51] To find the simulation temperature corresponding best to experiments, we calculate the J-coupling constants, $^3J_{H_N H_\alpha}$, of Aβ_{40} and Aβ_{42} at 300 and 325 K (the highest temperature before transition to random coil) and compare those with experimental J-coupling constants measured at 300 K.[28] We also examine the use of three sets of parameters for the Karplus equation (namely the Vuister's,[59] Sgourakis',[35] and Schmidt's[60] parameter sets) in calculating the J-coupling constants from the simulations.

Figure 2 superposes the J-coupling constants calculated for both alloforms at 300 and 325 K using the Vuister's parameter set[59] on the experimental values.[28] In the inset, the Vuister's parameter set is compared to that proposed recently by Sgourakis et al.[35] for the simulations at 325 K. Qualitatively, both temperature data sets follow the same trend for Aβ_{40} and Aβ_{42}. We note, however, for the Vuister's set, an overall J-coupling shift in the N-terminal region for Aβ_{40} compared to experiment, a shift that is considerably reduced with Sgourakis' set. Quantitatively (Table 1), the Pearson correlation coefficient (PCC) remains nearly the same for Aβ_{40} independently of the simulation temperature and the parameter set used but is significantly improved for Aβ_{42} at 325 K, indicating that this latter temperature is most relevant for comparison with experiment.

Using the same residues and experimental J-coupling constant values[28] as benchmark, our results can be compared to the PCC obtained by other computational studies. For Aβ_{42}, our PCC value of 0.43 agrees with the values derived from all-atom REMD simulations in explicit solvent using OPLS (PCC of 0.43 using 60 ns per replica) and AMBER99SB (PCC of 0.4−0.5 using

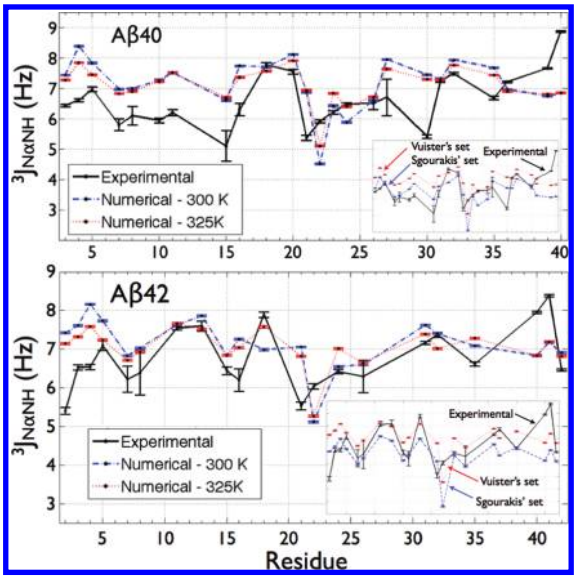

Figure 2. J-coupling constants $^3J_{H_\alpha H_N}$ for Aβ_{40} and Aβ_{42} at 300 and 325 K. The J-coupling constants determined experimentally[28] for Aβ_{40} and Aβ_{42} are compared to the predicted J-coupling constants obtained in our simulations. The inset in each figure compares experiment[28] (black curve) and the numerically predicted J-coupling constants at 325 K using Sgourakis'[35] and Vuister's[59] (blue and red curves, respectively) parameter sets in Karplus equation.[58] Glycine residues are not included because their experimental values are ambiguous.

Table 1. PCC between Experimental and Calculated J-Coupling Constants[a]

	Vuister et al.[59]		Sgourakis et al.[35]		Schmidt et al.[60]	
parameter set	all	part	all	part	all	part
Aβ_{40} - 325K	0.28	0.45	0.29	0.57	0.29	0.57
Aβ_{40} - 300K	0.26	0.40	0.27	0.53	0.27	0.50
Aβ_{42} - 325K	0.43	0.65	0.42	0.72	0.43	0.71
Aβ_{42} - 300K	0.27	0.52	0.29	0.39	0.27	0.44

[a] Glycine residues are not included because their experimental values are ambiguous. The first and the second columns for each parameter set contain, respectively, the PCC obtained when using all the data points and when neglecting the four most problematic residues. For Aβ_{40}, we neglected residues 15, 21, 30, and 40 when using Vuister et al.,[59] residues 22, 30, 39, and 40 when using Sgourakis et al.,[35] and residues 22, 30, 39, and 40 when using Schmidt et al.[60] parameter sets. For Aβ_{42}, we neglected residues 2, 21, 40, and 41 when using Vuister et al., residues 2, 22, 40, and 41 when using Sgourakis et al., and residues 2, 22, 40, and 41 when using Schmidt et al. parameter sets.

225 ns per replica) force fields.[28,35] For Aβ_{40}, our PCC value of 0.29 is lower than that obtained by all-atom REMD using OPLS (PCC of 0.66) but is similar to that obtained using all-atom REMD with the AMBER96 force field (PCC of 0.27).[28] Our moderate correlation for Aβ_{40} is due a shift of more than ~1 Hz for most of the N-terminal residues and the four outliers at positions Glu22, Ala30, Val39, and Val40.

Though there is no physical rational for eliminating outliers, to compare with Mitternacht et al.,[34] we follow their procedure and eliminate the four most significant outliers out of the 24 and 21 experimental data points for Aβ_{40} and Aβ_{42}, respectively, and compute the PCC using the Schmidt's parameters set.[60] Doing

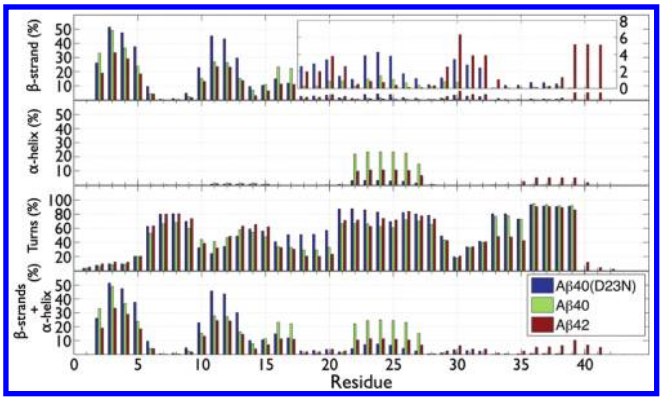

Figure 3. Per residue secondary structure propensities. From top to bottom: β-strand, α-helix, turn, and α-helix plus β-strand propensities in percentage (%). Aβ_{40} is shown in green, Aβ_{42} in red, and Aβ_{40}(D23N) in blue.

so, our PCCs increase from 0.29 to 0.57 for Aβ_{40} and from 0.43 to 0.71 for Aβ_{42}, showing that only a few outlying points strongly impact the PCC (Table 1). Using the same approach, our PCC for Aβ_{42}, 0.71 is comparable to the PCC of 0.86 determined by Mitternacht et al.[34]

3.2. Aβ_{40} Properties. *Secondary Structure.* Averaged over all structures and residues, Aβ_{40} has 7.7 ± 0.1% β-strand, 3.4 ± 0.1% α-helix, 50.2 ± 0.1% turn, and 38.8 ± 0.1% random coil. Compared to a recent CD study on Aβ_{40} (8% α-helix and 24% β-strand),[32] our ensemble shows a comparable propensity for α-helices but underestimates the percentage of β-strands. This experiment, however, may overestimate the percentage of β-strands because NMR shows a very weak signal,[13,16] and an earlier CD experiment using a more stringent sample separation protocol reports only ~12% of β-strands.[3]

The secondary structure propensities for each residue in Aβ_{40} are shown in Figure 3. Three β-strands are present from Ala2 to Arg5 with a propensity of 20−50%, from Glu10 to His13 and Lys16 to Leu17 with a propensity of 15−30%, and from Phe18 to Ala30 with a small propensity (<1%). The first two β-strands are stabilized by turns at His6-Gly9 and His13-Gln15. The β-strands 2 and 3 are found in competition with 2 α-helices spanning Glu11-Gln15 with a small probability (<1%) and Glu22-Asn27 with a probability of up to 25%, as depicted in Figure 3. Finally, our analysis also shows a high turn signal (>60%) between residues 21 and 28 and between residues 33 and 39.

Tertiary Structure. Several contacts play a dominant role in the tertiary structure of Aβ_{40}, as shown in Figure 4. The C-terminal interacts with the CHC forming hydrophobic contacts between Leu34-Phe19, Val36-Phe19, Met35-Phe19, and Met35-Phe20 with high probabilities and between Ile31-Ile32 and Val18 with slightly lower probabilities. We also observe hydrophobic contacts localized in the CHC between Leu17-Phe19 and Val18-Phe20, indicating a mostly collapsed core. We also find that the electrostatic Asp23-Lys28 contact, present in about 65% of the morphologies, stabilizes a turn between Ala21 and Lys28.

Column 1 of Figure 5 shows the center of the five dominant Aβ_{40} clusters with their respective populations. These five clusters contain 34.3% of all generated conformations. The center of cluster 1 is fully random coil. The centers of clusters 2−5 display two β-strands at the N-terminal residues 2−4 and 10−12, leading to a well-formed or a very flexible β-hairpin for the clusters 4−5 and 2−3, respectively. While the cluster centers do

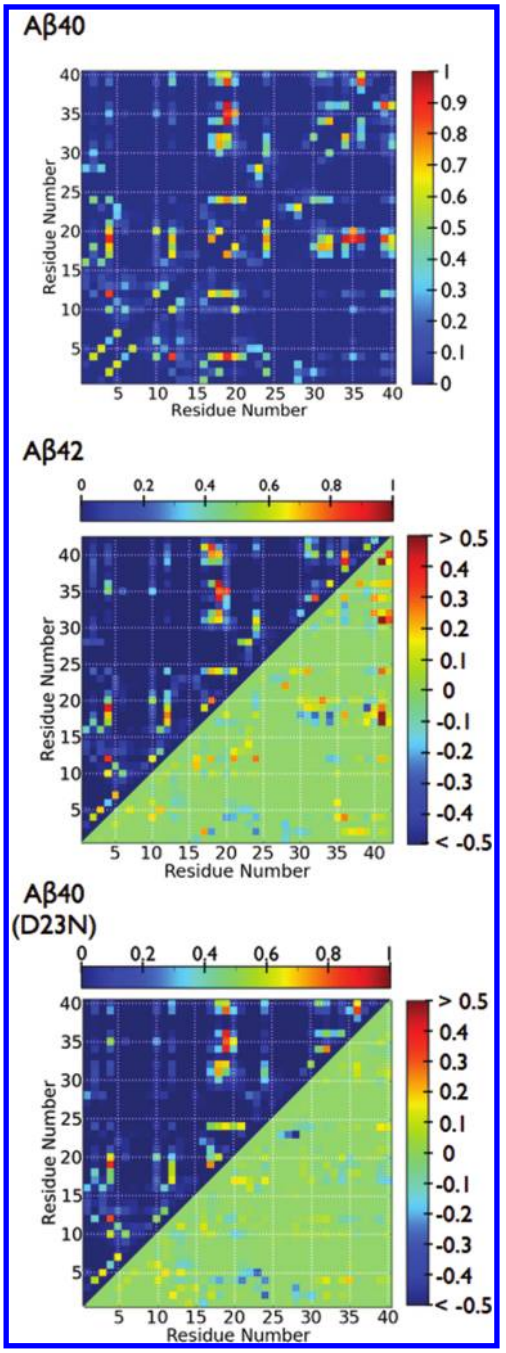

Figure 4. Contact maps between side chains. The contact maps of Aβ_{40}, Aβ_{42} and Aβ_{40}(D23N) are shown in the top, middle, and bottom panels, respectively. The upper left corner of each panel depicts the propensity of contact between side chains in each alloform. The lower right corner for Aβ_{42} and Aβ_{40}(D23N) displays the contact differences between each alloform and Aβ_{40}. When there is more contacts in Aβ_{40}, the propensity is negative (blueish), and the opposite yields a positive propensity (reddish).

not exhibit secondary structure in the CHC or the C-terminal, the loop region is structurally near a α-helical conformation, and we find a α-helix at residues 22−26 with ∼45% probability when averaging over all conformations belonging to the top three clusters. All five clusters display contacts between CHC and the C-terminal. Clusters 1−3 also show contacts between residues 1−15 and 21−38, while these contacts are absent in clusters 4 and 5.

3.3. Aβ_{42} Compared to Aβ_{40}. *Secondary Structure.* Averaged over all structures and residues, Aβ_{42} shows 2.1 ± 0.1% α-helix, 6.1 ± 0.1% β-strand, 48.3 ± 0.1% turn, and 43.4 ± 0.1% random coil contents, whereas Aβ_{40} exhibits 3.4 ± 0.1% α-helix, 7.7 ± 0.1% β-strand, 50.2 ± 0.1% turn, and 38.8 ± 0.1% random coil. Thus, these two sequences have the same overall secondary structure composition. It is in the propensity per residue that differences arise.

The secondary structure propensity for each residue is shown in Figure 3. As for Aβ_{40}, there are β-strands at the N-terminal at positions Ala2-Arg5, Glu10-His13, and Lys16-Val17, but their propensities are smaller in Aβ_{42}. Noticeably, Aβ_{42} is more prone than Aβ_{40} to form β-strands at the CHC and at positions Ala30-Ile32 and Val39-Ile41, as depicted by the inset in Figure 3. Thus, there is a small random coil to β-strand transition at the CHC and the C-terminal in going from Aβ_{40} to Aβ_{42}. Overall, 1.4% of Aβ_{40} and 8.6% of Aβ_{42} structures display β-strands at the CHC or C-terminal. As for Aβ_{40}, there are in Aβ_{42} two α-helices at positions Glu11-Gln15 and Glu22-Asn27 (Figure 3). The α-helix at Glu22-Asn27 is however reduced in going from Aβ_{40} (∼22%) to Aβ_{42} (∼10%). In addition, we find in Aβ_{42} a third helix at positions Met35-Val40 that is absent in Aβ_{40} (Figure 3). On the other hand, both alloform share a very similar turn profile.

Tertiary Structure. Many hydrophobic contacts contribute to the Aβ_{42} monomer morphologies. Most of them are also present in Aβ_{40}, as depicted in Figure 4 that shows the differences in the contact propensity between the two alloforms. These include a number of contacts between the CHC and the C-terminal, particularly between Met35 and the two residues Phe19 and Phe20. The hydrophobic residue Ile41 increases the overall contact occurrence between the CHC and the C-terminal by interacting predominantly with Leu17 and Val18. It also increases contacts inside the C-terminal itself. Finally, the addition of Ile41 and Ala42 causes a small shift of the interactions between the N-terminal and the region 15−35 toward the C-terminal or the N-terminal. This shift may allow the conformational freedom necessary for the CHC to form β-strands and for the region 22−29 to form more easily the specific loop conformation required for fibrillation. Electrostatic interactions also play a role in Aβ_{42} structures. Aβ_{42} and Aβ_{40} have approximately the same propensity of forming a contact between Asp23 and Lys28 (∼ 60%) with a similar contact distance distribution (data not shown).

While the probability of contact occurrence differs between Aβ_{40} and Aβ_{42}, both alloforms have a very similar conformational ensemble, and only 16% of all Aβ_{42} conformations are unique, i.e., show a C_α-rmsd greater than 2 Å from any observed Aβ_{40} structures by using residues 1−40. The centers of the five dominant Aβ_{42} clusters are shown in column 2 of Figure 5. These five clusters include 50.1% of all conformations. We observe that some of these clusters are structurally similar to the main clusters of Aβ_{40}. For instance, clusters 2 and 4 of Aβ_{42} are respectively similar to clusters 2 and 5 of Aβ_{40}. The third cluster is similar to the cluster 6 of Aβ_{40} that represents 1.2% of its structural ensemble. On the other hand, the first cluster of Aβ_{42} is only similar to marginal clusters of Aβ_{40} (<1%), and its fifth cluster is not present in Aβ_{40}.

To identify the structural differences between Aβ_{42} and Aβ_{40}, we cluster all unique structures of Aβ_{42}. The first five unique clusters of Aβ_{42} are shown in column 4 of Figure 5 and represent 6% of all generated conformations. We observe that these Aβ_{42} unique morphologies display β-strands at the C-terminal and CHC. In particular, the first, third, and fifth unique clusters show

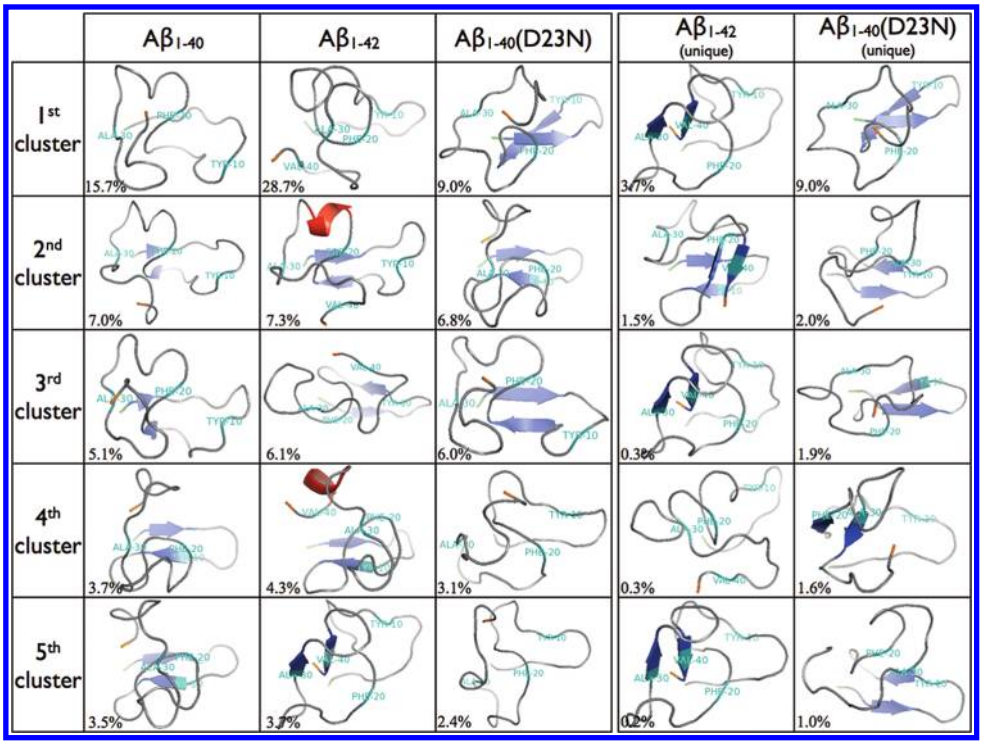

Figure 5. Clusters centers. Centers of the five dominant clusters for Aβ_{40} (first column), Aβ_{42} (second column), and Aβ_{40}(D23N) (third column). The fourth and fifth columns contain, respectively, the centers of the five dominant clusters of Aβ_{42} and Aβ_{40}(D23N) unique morphologies. The percentages shown are with respect to the total number of structures analyzed. The secondary structure was assigned using STRIDE.[55] The N- and C-termini are shown in green and orange, respectively, for all alloforms, Tyr10, Phe20, Ala30, and Val40, and for Aβ_{42} only, are shown in teal.

a β-hairpin motif with strands spanning the C-terminal at residues 30−32 and 39−41. Structurally, these three clusters are near each other differing only at the N-terminal. Another interesting motif is seen in the second unique cluster, where we note that the extremity of the C-terminal may also interact with the CHC forming a β-sheet between residues 18−20 and 39−41.

3.4. Aβ_{40}(D23N) Compared to Aβ_{40}. *Secondary Structure.* Averaged over all structures and residues, Aβ_{40}(D23N is composed of 10.1 ± 0.1% β-strand vs 7.7 ± 0.1% in Aβ_{40}, 0.5 ± 0.1% α-helix vs 3.4 ± 0.1% in Aβ_{40}, 56.2 ± 0.1% turn, which is 6.0% higher than in Aβ_{40}, and 33.2 ± 0.1% random coil.

Differences are also observed in the per residue secondary structure, as shown in Figure 3. For example, the β-strand propensity of residues Tyr10-His14 is higher in Aβ_{40}(D23N) than in Aβ_{40} causing a lower β-strand propensity at Gln15-Leu17. Aβ_{40}(D23N) and Aβ_{42} show similar β-strand propensities at positions Val18-Ala21 and Ala30-Ile32 that are absent in Aβ_{40}(Figure 3). Overall, 5.0% of Aβ_{40}(D23N) structures vs 1.4% of Aβ_{40} structures display β-strands at the CHC and the C-terminal. From our simulations, we also see that Aβ_{40}(D23N) has a negligible propensity for α-helical configurations, with a small signal at positions 22−27, a feature that may favor a faster appearance of fibril-compatible intermediate oligomers with β-strands at the CHC and the C-terminal in Aβ_{40}(D23N) than in Aβ_{40}.

The turn propensity in the N-terminal, at His6-Gly9 and His13-Gln15, is very similar to Aβ_{40} and Aβ_{42}. Differences are however observed for the CHC, the loop, region and the C-terminal. At the CHC, residues 17−20 have a propensity for turn of ∼50%, which is higher than in Aβ_{40} and Aβ_{42} by ∼20−30%, resulting in less random coils. The C-terminal also exhibits a higher propensity for turn in Aβ_{40} and Aβ_{40}(D23N) than in Aβ_{42}, particularly at residues 33−35, generating a longer turn extending from residues 33 to 39. Finally, the loop region has a higher propensity for turn in Aβ_{40}(D23N) than in the wild-type alloforms, and the contacts that stabilize this region are very different from Aβ_{40} as described below.

Tertiary Structure. While 16% of Aβ_{42} conformations differ from any observed Aβ_{40} conformations, cluster analysis reveals that 35% of Aβ_{40}(D23N) conformations are distinct from those obtained for Aβ_{40} (C_α-rmsd >2 Å). Differences in the contact distribution between Aβ_{40} and Aβ_{40}(D23N) are shown in Figure 4. For instance, there is a shift of the contacts between the N-terminal and the residues 15−30 toward the C- or N-terminal. While this shift is qualitatively similar to what occurs in Aβ_{42} as described previously, the overall reduction in contacts is more important in Aβ_{40}(D23N). The N-terminal of Aβ_{40}-(D23N) looses many contacts with the region 15−30 without recovering them all with the C-terminal, as shown by Figure 4, allowing more conformational freedom. Another main difference is observed for the Asp(Asn)23-Lys28 contact propensity which is reduced by 54% in going from Aβ_{40}(D23N) to Aβ_{40} (Figure 4). This induces a rich polymorphism for the region between Ala21 and Ala30 as opposed to the other two alloforms studied. Noticeably, the side chains of Asn23 and Lys28 in Aβ_{40}(D23N) are then unconstrained as they do not form other significant contacts (Figure 4).

The centers of the five dominant clusters of Aβ_{40}(D23N) are displayed in the third column of Figure 5. These represent 27.3% of all generated conformations. As for Aβ_{40}, they are mostly disordered without any β-strands at the CHC or C-terminal as could be expected, since 65% of Aβ_{40}(D23N) and Aβ_{40}

conformations are structurally similar (C_α-rmsd < 2 Å). For instance, the centers of the clusters 2 and 3 of Aβ_{40}(D23N) are similar to the centers of the clusters 4 and 1 of Aβ_{40}, respectively. On the other hand, cluster 4 of Aβ_{40}(D23N) is only similar to Aβ_{40} marginal clusters (<1%), and its first cluster is not found in the structural ensemble of Aβ_{40}.

The Aβ_{40}(D23N) unique clusters are shown in the fifth column of Figure 5. The first unique cluster, which has a population of 9%, is also the most dominant cluster for this sequence (see column 3). In term of secondary structure, this cluster is rather unstructured with β-strands only at residues 2−5 and 11−16. The fourth unique cluster displays a β-sheet between residues 18−20 and 30−32 and represents 1.6% of all visited structures. While the other Aβ_{40}(D23N) unique clusters are as unstructured as Aβ_{40}, their contact distributions differ in two notable ways: (1) Their N-terminals can be isolated from the loop region and interact less with the CHC (unique clusters 1 and 3); their contact maps show very few contact between residues 1−15 and 22−29 and between residues 5−15 and 14−21 (data not shown), or (2) these unique clusters can have few contacts between residues 1−9 and 22−40 (unique clusters 2 and 5). For these two latter unique clusters, we note also that they exhibit electrostatic interactions between the positively charged Lys28 and the negatively charged Glu11, as Lys28 now interacts very weakly with Asn23 as opposed to wild-type. Overall, these unique morphologies do not have contacts between the N-terminal and the loop region allowing Aβ_{40}(D23N) to be less compact than Aβ_{40}.

4. DISCUSSION

Knowledge of the Aβ conformations at the monomer level in aqueous solution is of utmost importance since the monomer interacts with higher order oligomers[6] and fibrils[19] and is a building block of the cytotoxic dimer.[21] Both Aβ_{40} and Aβ_{42} monomers have been studied by NMR, CD, and computer simulations. Results show that these peptides are described by a distinct ensemble of predominantly random coil structures. While many simulations were performed,[29] very few showed thorough sampling of the relevant morphological ensemble.[34,35] The similarities and differences of our results with previous experiments and simulations on the Aβ_{40} and Aβ_{42} monomers can be summarized as follows.

Our contact distributions of Aβ_{40} and Aβ_{42} can be compared to the previous all-atom implicit solvent simulation results obtained by Yang and Teplow.[29] We note two differences. First, while we observe a fourth region between residues 30 and 40 in which intraregion contacts are important for both Aβ_{40} and Aβ_{42}, the role of this region was only identified for Aβ_{42} by Yang and Teplow. Second, there is a slight shift in the contacts between the N-terminal and the loop region. If these regions were seen to interact by contacts between residues 6−10 and 22−28 in the simulations of Yang and Teplow,[29] our results show interactions between residues 1−5 and 16−28 (Figure 4). On the other hand, both simulations agree on several points: the N-terminal interaction with the loop region, the increased number of contacts between the CHC and the C-terminal for Aβ_{42}, the presence of more localized contacts at the C-terminal for Aβ_{42}, and the fact that intraregion contacts are more dominant in the four regions corresponding to the turn distribution observed in Figure 3.

Inspection of the four sequence regions show interesting features. We find that the N-terminal (residues 1−16) of the two wild-type alloforms is very similar with turns at His6-Gly9 and His13-Gln15, stabilizing extended morphologies having β-strands. A weak turn was also observed at Asp7-Glu11 by NMR,[16] and two turns were predicted at His6-Gly9 and His14-Lys16 using all-atom REMD simulations.[28,29] On the other hand, the presence of β-strands at the N-terminal of Aβ_{40} is clearly a matter of debate from experimental and computational studies. While some experiments show that the N-terminal of Aβ_{40} monomer may form β-strands,[63] others observe that it is extended and highly fluctuating[14,17] without any β-strands.[16] Three all-atom REMD simulations report either negligible[28] or low[29,35] β-strand percentages. In contrast, coarse-grained DMD simulations report a propensity for β-strand of ∼40% at Ala2-Phe4.[64] Taken together, all these studies suggest that the N-terminal may be in rapid exchange between an extended−turn−extended motif free of any H-bonds and β-stranded configurations, with a turn at His6-Gly9 being formed most of the time, as shown in our study by the propensities in Figure 3. We find that Aβ_{42} has also a non-negligible probability to populate a β-hairpin at the N-terminal, a motif that has been predicted recently with two different all-atom potentials.[34,35] This motif has however a lower probability in Aβ_{42} than in Aβ_{40}. This motif, which was not observed experimentally yet due to its low population, might have consequences on the early formed Aβ_{42} oligomers.

The formation of a loop region between residues 22−29 stabilized by a salt bridge between Asp23-Lys28 is thought to be one of the rate-limiting steps of Aβ_{40} fibrillation.[65] Recently, the formation of this contact was shown to increase the population of competent fibril-like monomers for Aβ_{10-35}.[26] Here, we observe many morphologies with a turn between Ala21 and Lys28 stabilized by interactions between the side chains of Asp23 and Lys28 in the wild-type sequences (Figures 3 and 4), with a probability of ∼65%. This turn was suggested from proteolysis experiment on the Aβ_{40} monomer,[18] and its morphology was resolved at the molecular level using solution NMR of the Aβ_{21-30} peptide.[18] The turn ensemble of residues 22−28 for Aβ_{40}, in our simulation, is marginally similar to the two NMR conformations of the Aβ_{21-30} peptide with 20% of our conformations deviating by less than 1.5 Å. These differences can be explained by the presence of contacts between the N-terminal and the loop region with ∼35% probabilities (Figure 4). Overall, our results on Aβ_{40} are consistent with experiments on the Aβ_{40} monomer showing turns at positions 23−29,[14] 20−26,[16] or 24−28.[18] Our results on Aβ_{40} also agree with previous REMD simulations on the Aβ_{40} monomer[29] and MD simulations on the Aβ_{10-35} monomer and dimer[26] that suggest that the loop region, residues 22−29, needs to undergo structural changes during fibrillation, leading to further stabilization of the Asp23-Lys28 contact.

The CHC (residues 17−21) and the C-terminal (residues 30−42) are recognized experimentally as the driving regions for aggregation through the formation of β-stranded and extended structures.[66−68] Experiments revealed that the C-terminal of Aβ_{42} monomer is more rigid than that of Aβ_{40}[15] and displays β-strands at residues Val39-Ile41.[14,16] Previous simulations also observed a more structured C-terminal in Aβ_{42} than in Aβ_{40}.[28,29,35,64] In agreement with these experiments and simulations, we observe in our study that the C-terminal residues Ala39-Ile41 modulate, by direct interactions, the appearance of distinct Aβ_{42} morphologies with β-strands at the CHC and the C-terminal that are absent in the Aβ_{40} ensemble. We isolated these morphologies which exhibit a β-sheet between residues 39−41

and 30−32 or between residues 39−41 and 18−20 (see fourth column in Figure 5). Our results emphasize the important role of Ile41-Ala42 in the monomer morphologies, and its role in the early oligomerization process as was observed experimentally.[3,69]

Our findings on the aggregation prone mutant D23N can be summarized as follows. $A\beta_{40}$(D23N) appears to form a more stable β-hairpin than the two wild-type peptides, as a significant portion of their N-terminal structures. As could be expected, $A\beta_{40}$(D23N) monomer does not exhibit any significant interaction between Asn23 and Lys28. This region displays rather a high conformational flexibility giving the D23N alloform more freedom to adopt the loop conformations observed in its fibrillar states[39] and therefore reducing the free energy barriers. Interestingly, solid-state NMR indicates that $A\beta_{40}$(D23N) forms fibrils with multiple morphologies, with a majority having antiparallel β-sheets and a minority having parallel β-sheets.[39] From our simulations, we see that this wide polymorphism may originate in part from the unconstrained side chains of Asn23 and Lys28, the flexibility of the region 21−29, and their overall consequences on $A\beta_{40}$(D23N) equilibrium ensembles.

Our results show that, while $A\beta_{40}$(D23N) does not contain Ile41, the mutation D23N increases the β-strand content at the CHC and the C-terminal when compared to $A\beta_{40}$ (Figure 3). Specifically, one of our unique $A\beta_{40}$(D23N) morphologies displays a β-sheet between residues 18−20 and 30−32 (fifth column in Figure 5). Even if its weight of 1.6% is small, this motif is interesting as it involves two regions known to be crucial during oligomerization.[6,66,67]

The higher propensity of $A\beta_{40}$(D23N) monomer to form β-strands at the CHC and the C-terminal and to prefer less collapsed topologies than $A\beta_{40}$ monomer suggests important consequences on its dock-and-lock mechanism when it binds to fibril edge. Previous simulations on the $A\beta_{10-40}$ monomer at the edge of a preformed fibril showed that the fibril edge induces a conversion of the CHC to β-stranded configurations in the monomer.[31,70] In another computational study, interactions between the C-terminal peptide Met35-Val40 and a fibril were simulated showing a transition of the peptide from random coil to extended configuration upon binding to fibril edge.[71] Taken together, our results suggest that $A\beta_{40}$(D23N) may exhibit easier conversion to extended configuration upon binding to the fibril edge and therefore increases its fibril elongation rate.

Finally, it was observed using photoinduced cross-linking experiments that D23N promotes the formation of high-order oligomers when compared with wild-type $A\beta_{40}$.[6] High-order oligomers are also formed by $A\beta_{42}$, which preferably forms pentamer and hexamer, in contrast to $A\beta_{40}$, which forms low-order oligomers, such as monomers to tetramers in rapid equilibrium.[6] In our simulation, we observe that both $A\beta_{42}$ and $A\beta_{40}$(D23N) monomers exhibit a noticeable reduction of contacts between the N-terminal and the residues 22−29 and between the N-terminal and the residues 18−21 of the CHC (Figure 4), a feature that could favor the appearance of high-order oligomers by freeing the segment 22−29 and the CHC.

5. CONCLUSION

In this study, we have revisited the structures of the $A\beta_{40}$ and $A\beta_{42}$ monomers using the OPEP force field and the HT-REMD technique and provided for the first time the structures of the peculiar $A\beta_{1-40}$(D23N) monomer, which self-assembles without any lag phase to predominant amyloid fibrils with antiparallel β-sheets.[39]

We observe that even if these three alloforms are mostly disordered at the monomeric level, in agreement with experiments and previous simulations on $A\beta_{1-40}$ and $A\beta_{1-42}$, striking morphological differences exist. For instance, $A\beta_{1-42}$ has higher β-hairpin propensities at the C-terminal, residues 30−42, than that of $A\beta_{1-40}$. Moreover, 16% of all $A\beta_{1-42}$ conformations do not ressemble to any $A\beta_{1-40}$ conformations.

The monomeric morphological ensemble of $A\beta_{40}$(D23N) also presents significantly different from that of $A\beta_{40}$ with 35% of unique conformations. In particular, we observe a β-hairpin-like motif between residues 18−20 and 30−32 in $A\beta_{1-40}$-(D23N) that is not present in $A\beta_{1-40}$. Moreover, D23N enhances the conformational freedom of residues 22−30. It changes the network of contacts, the N-terminal becoming more independent from the rest of the protein, leading to less compact morphologies than the wild-type $A\beta_{1-40}$ peptide. These structural properties could explain why the kinetics and the final amyloid products vary so extensively between the $A\beta_{1-40}$ and $A\beta_{40}$(D23N) peptides, by increasing the population of the amyloid-competent monomeric state.

AUTHOR INFORMATION

Corresponding Author

*E-mail: normand.mousseau@umontreal.ca.

ACKNOWLEDGMENT

This work was funded in part by the Canada Research Chairs program, the Fonds québécois de recherche sur la nature et les technologies (FQRNT), the Natural Sciences and Engineering Reasearch Council of Canada (NSERC), and the Fonds de recherche en santé du Québec (FRSQ). Calculations were done on the computers of the Réseau québécois de calcul de haute performance. Financial support of CNRS and the Institut Universitaire de France is also acknowledged.

REFERENCES

(1) Selkoe, J. D. *Nature* **2003**, *426*, 900–904.
(2) Haass, C.; Selkoe, D. J. *Nat. Rev. Mol. Cell Biol.* **2007**, *8*, 101–112.
(3) Kirkitadze, M. D.; Condron, M. M.; Teplow, D. B. *J. Mol. Biol.* **2001**, *312*, 1103–1119.
(4) Olofsson, A.; Lindhagen-Persson, M.; Sauer-Eriksson, A. E.; Ohman, A. *Biochem. J.* **2007**, *404*, 63–70.
(5) Petkova, A. T.; Leapman, R. D.; Guo, Z.; Yau, W.-M.; Mattson, M. P.; Tycko, R. *Science* **2005**, *307*, 262–265.
(6) Bitan, G.; Kirkitadze, M. D.; Lomakin, A.; Vollers, S. S.; Benedek, G. B.; Teplow, D. B. *PNAS* **2003**, *100*, 330–335.
(7) Chen, Y.-R.; Glabe, C. G. *J. Biol. Chem.* **2006**, *281*, 24414–24422.
(8) Lublin, A. L.; Gandy, S. *Mt. Sinai J. Med.* **2010**, *77*, 43–49.
(9) Sakono, M.; Zako, T. *FEBS J.* **2010**, *277*, 1348–1358.
(10) Faller, P. *ChemBioChem* **2009**, *10*, 2837–2845.
(11) Bokvist, M.; Lindstrom, F.; Watts, A.; Grobner, G. *J. Mol. Biol.* **2004**, *335*, 1039–1049.
(12) Selkoe, J. D. *Behav. Brain Res.* **2008**, *192*, 106–113.
(13) Zhang, S.; Iwata, K.; Lachenmann, M. J.; Peng, J. W.; Li, S.; Stimson, E. R.; Lu, Y.-a.; Felix, A. M.; Maggio, J. E.; Lee, J. P. *J. Struct. Biol.* **2000**, *130*, 130–141.
(14) Lim, K. H.; Collver, H. H.; Le, Y. T. H.; Nagchowdhuri, P.; Kenney, J. M. *Biochem. Biophys. Res. Commun.* **2007**, *353*, 443–449.
(15) Yan, Y.; Wang, C. *J. Mol. Biol.* **2006**, *364*, 853–862.

(16) Hou, L.; Shao, H.; Zhang, Y.; Li, H.; Menon, N. K.; Neuhaus, E. B.; Brewer, J. M.; Byeon, I.-J. L.; Ray, D.; Vitek, M. P.; Iwashita, T.; Makula, R. A.; Przybyla, A. B.; Zagorski, M. G. *J. Am. Chem. Soc.* **2004**, *126*, 1992–2005.
(17) Zhang, A.; Qi, W.; Good, T. A.; Fernandez, E. J. *Biophys. J.* **2009**, *96*, 1091–1104.
(18) Lazo, N. D.; Grant, M. A.; Condron, M. C.; Rigby, A. C.; Teplow, D. B. *Protein Sci.* **2005**, *14*, 1581–1596.
(19) Esler, W. P.; Stimson, E. R.; Jennings, J. M.; Vinters, H. V.; Ghilardi, J. R.; Lee, J. P.; Mantyh, P. W.; Maggio, J. E. *Biochemistry* **2000**, *39*, 6288–6295.
(20) Giuffrida, M. L.; Caraci, F.; Pignataro, B.; Cataldo, S.; De Bona, P.; Bruno, V.; Molinaro, G.; Pappalardo, G.; Messina, A.; Palmigiano, A.; Garozzo, D.; Nicoletti, F.; Rizzarelli, E.; Copani, A. *J. Neurosci.* **2009**, *29*, 10582–10587.
(21) Shankar, G. M.; Li, S.; Mehta, T. H.; Garcia-Munoz, A.; Shepardson, N. E.; Smith, I.; Brett, F. M.; Farrell, M. A.; Rowan, M. J.; Lemere, C. A.; Regan, C. M.; Walsh, D. M.; Sabatini, B. L.; Selkoe, D. J. *Nat. Med.* **2008**, *14*, 837–842.
(22) Xu, Y.; Shen, J.; Luo, X.; Zhu, W.; Chen, K.; Ma, J.; Jiang, H. *Proc. Natl. Acad. Sci. U.S.A.* **2005**, *102*, 5403–5407.
(23) Flock, D.; Colacino, S.; Colombo, G.; Di Nola, A. *Proteins* **2006**, *62*, 183–192.
(24) Raffa, D. F.; Rauk, A. *J. Phys. Chem. B* **2007**, *111*, 3789–3799.
(25) Triguero, L.; Singh, R.; Prabhakar, R. *J. Phys. Chem. B* **2008**, *112*, 7123–7131.
(26) Reddy, G.; Straub, J. E.; Thirumalai, D. *J. Phys. Chem. B* **2009**, *113*, 1162–1172.
(27) Sugita, Y.; Okamoto, Y. *Chem. Phys. Lett.* **1999**, *314*, 141–151.
(28) Sgourakis, N. G.; Yan, Y.; McCallum, S.; Wang, C.; Garcia, A. E. *J. Mol. Biol.* **2007**, *368*, 1448–1457.
(29) Yang, M.; Teplow, D. B. *J. Mol. Biol.* **2008**, *384*, 450–464.
(30) Anand, P.; Nandel, F. S.; Hansmann, U. H. E. *J. Chem. Phys.* **2008**, *129*, 195102.
(31) Takeda, T.; Klimov, D. K. *Proteins* **2009**, *77*, 1–13.
(32) Ono, K.; Condron, M. M.; Teplow, D. B. *PNAS* **2009**, *106*, 14745–14750.
(33) Ono, K.; Condron, M. M.; Teplow, D. B. *J. Biol. Chem.* **2010**, *285*, 23186–23197.
(34) Mitternacht, S.; Staneva, I.; Hard, T.; Irback, A. *Proteins* **2010**, *78*, 2600–2608.
(35) Sgourakis, N. G.; Merced-Serrano, M.; Boutsidis, C.; Drineas, P.; Du, Z.; Wang, C.; Garcia, A. E. *J. Mol. Biol.* **2011**, *405*, 570–583.
(36) Maupetit, J.; Tuffery, P.; Derreumaux, P. *Proteins* **2007**, *69*, 394–408.
(37) Laghaei, R.; Mousseau, N.; Wei, G. *J. Phys. Chem. B* **2010**, *114*, 7071–7077.
(38) Grabowski, T. J.; Cho, H. S.; Vonsattel, J. P. G.; Rebeck, G. W.; Greenberg, S. M. *Ann. Neurol.* **2001**, *49*, 697–705.
(39) Tycko, R.; Sciarretta, K. L.; Orgel, J. P. R. O.; Meredith, S. C. *Biochemistry* **2009**, *48*, 6072–6084.
(40) Petkova, A. T.; Ishii, Y.; Balbach, J. J.; Antzutkin, O. N.; Leapman, R. D.; Delaglio, F.; Tycko, R. *Proc. Natl. Acad. Sci. U.S.A.* **2002**, *99*, 16742–16747.
(41) Luhrs, T.; Ritter, C.; Adrian, M.; Riek-Loher, D.; Bohrmann, B.; Dobeli, H.; Schubert, D.; Riek, R. *PNAS* **2005**, *102*, 17342–17347.
(42) Tycko, R. *Q. Rev. Biophys.* **2006**, *39*, 1–55.
(43) Andersen, H. C. *J. Comput. Phys.* **1983**, *52*, 24–34.
(44) Berendsen, H. J. C.; Postma, J. P. M.; van Gunsteren, W. F.; DiNola, A.; Haak, J. R. *J. Chem. Phys.* **1984**, *81*, 3684–3690.
(45) Chebaro, Y.; Dong, X.; Laghaei, R.; Derreumaux, P.; Mousseau, N. *J. Phys. Chem. B* **2009**, *113*, 267–274.
(46) Lu, Y.; Derreumaux, P.; Guo, Z.; Mousseau, N.; Wei, G. *Proteins* **2009**, *75*, 954–963.
(47) Laghaei, R.; Mousseau, N. *J. Chem. Phys.* **2010**, *132*, 165102.
(48) Liang, C.; Derreumaux, P.; Mousseau, N.; Wei, G. *Biophys. J.* **2008**, *95*, 510–517.
(49) Chen, W.; Mousseau, N.; Derreumaux, P. *J. Chem. Phys.* **2006**, *125*, 084911.
(50) Dong, X.; Chen, W.; Mousseau, N.; Derreumaux, P. *J. Chem. Phys.* **2008**, *128*, 125108.
(51) Chebaro, Y.; Mousseau, N.; Derreumaux, P. *J. Phys. Chem. B* **2009**, *113*, 7668–7675.
(52) Maupetit, J.; Derreumaux, P.; Tuffery, P. *J. Comput. Chem.* **2010**, *31*, 726–738.
(53) Maupetit, J.; Derreumaux, P.; Tuffery, P. *Nucleic Acids Res.* **2009 Jul 1**, *37* (Web Server issue), W498−503.
(54) Fukunishi, H.; Watanabe, O.; Takada, S. *J. Chem. Phys.* **2002**, *116*, 9058–9067.
(55) Frishman, D.; Argos, P. *Proteins: Struct., Funct., Genet.* **1995**, *23*, 566–579.
(56) Daura, X.; Suter, R.; van Gunsteren, W. F. *J. Chem. Phys.* **1999**, *110*, 3049–3055.
(57) Chodera, J. D.; Swope, W. C.; Pitera, J. W.; Seok, C.; Dill, K. A. *J. Chem. Theory Comput.* **2007**, *3*, 26–41.
(58) Karplus, M.; Anderson, D. H. *J. Chem. Phys.* **1959**, *30*, 6–10.
(59) Vuister, G. W.; Bax, A. *J. Am. Chem. Soc.* **1993**, *115*, 7772–7777.
(60) Schmidt, J. M.; Blumel, M.; Lohr, F.; Ruterjans, H. *J. Biomol. NMR* **1999**, *14*, 1–12.
(61) Newman, M. E. J.; Barkema, G. T. *Monte Carlo Methods in Statistical Physics*; Oxford University Press: Oxford, UK, 1999; 499 pages.
(62) Shaw, D. E.; Maragakis, P.; Lindorff-Larsen, K.; Piana, S.; Dror, R. O.; Eastwood, M. P.; Bank, J. A.; Jumper, J. M.; Salmon, J. K.; Shan, Y.; Wriggers, W. *Science* **2010**, *330*, 341–346.
(63) Danielsson, J.; Jarvet, J.; Damberg, P.; GrÃd'slund, A. *FEBS J.* **2005**, *272*, 3938–3949.
(64) Lam, A. R.; Teplow, D. B.; Stanley, H. E.; Urbanc, B. *J. Am. Chem. Soc.* **2008**, *130*, 17413–17422.
(65) Sciarretta, K. L.; Gordon, D. J.; Petkova, A. T.; Tycko, R.; Meredith, S. C. *Biochemistry* **2005**, *44*, 6003–6014.
(66) Liu, R.; McAllister, C.; Lyubchenko, Y.; Sierks, M. *J. Neurosci. Res.* **2004**, *75*, 162–171.
(67) Bernstein, S. L.; Wyttenbach, T.; Baumketner, A.; Shea, J.-E.; Bitan, G.; Teplow, D. B.; Bowers, M. T. *J. Am. Chem. Soc.* **2005**, *127*, 2075–2084.
(68) Melquiond, A.; Dong, X.; Mousseau, N.; Derreumaux, P. *Curr. Alzheimer Res.* **2008**, *5*, 244–250.
(69) Bitan, G.; Vollers, S. S.; Teplow, D. B. *J. Biol. Chem.* **2003**, *278*, 34882–34889.
(70) Takeda, T.; Klimov, D. K. *Biophys. J.* **2009**, *96*, 4428–4437.
(71) O'Brien, E. P.; Okamoto, Y.; Straub, J. E.; Brooks, B. R.; Thirumalai, D. *J. Phys. Chem. B* **2009**, *113*, 14421–14430.